J. Fluid Mech. (2007), *vol.* 589, *pp.* 1–31. © 2007 Cambridge University Press
doi:10.1017/S0022112007007823 Printed in the United Kingdom

Fluid flow and heat transfer in a dual-wet micro heat pipe

JIN ZHANG[1], STEPHEN J. WATSON[2] AND HARRIS WONG[1]†

[1]Department of Mechanical Engineering, Louisiana State University, Baton Rouge,
LA 70803-6413, USA

[2]Department of Mathematics, Louisiana State University, Baton Rouge, LA 70803-6413, USA

(Received 6 May 2006 and in revised form 16 May 2007)

Micro heat pipes have been used to cool micro electronic devices, but their heat transfer coefficients are low compared with those of conventional heat pipes. In this work, a dual-wet pipe is proposed as a model to study heat transfer in micro heat pipes. The dual-wet pipe has a long and narrow cavity of rectangular cross-section. The bottom-half of the horizontal pipe is made of a wetting material, and the top-half of a non-wetting material. A wetting liquid fills the bottom half of the cavity, while its vapour fills the rest. This configuration ensures that the liquid–vapour interface is pinned at the contact line. As one end of the pipe is heated, the liquid evaporates and increases the vapour pressure. The higher pressure drives the vapour to the cold end where the vapour condenses and releases the latent heat. The condensate moves along the bottom half of the pipe back to the hot end to complete the cycle. We solve the steady-flow problem assuming a small imposed temperature difference between the two ends of the pipe. This leads to skew-symmetric fluid flow and temperature distribution along the pipe so that we only need to focus on the evaporative half of the pipe. Since the pipe is slender, the axial flow gradients are much smaller than the cross-stream gradients. Thus, we can treat the evaporative flow in a cross-sectional plane as two-dimensional. This evaporative motion is governed by two dimensionless parameters: an evaporation number E defined as the ratio of the evaporative heat flux at the interface to the conductive heat flux in the liquid, and a Marangoni number M. The motion is solved in the limit $E \rightarrow \infty$ and $M \rightarrow \infty$. It is found that evaporation occurs mainly near the contact line in a small region of size $E^{-1}W$, where W is the half-width of the pipe. The non-dimensional evaporation rate $Q^* \sim E^{-1} \ln E$ as determined by matched asymptotic expansions. We use this result to derive analytical solutions for the temperature distribution T_p and vapour and liquid flows along the pipe. The solutions depend on three dimensionless parameters: the heat-pipe number H, which is the ratio of heat transfer by vapour flow to that by conduction in the pipe wall and liquid, the ratio R of viscous resistance of vapour flow to interfacial evaporation resistance, and the aspect ratio S. If $HR \gg 1$, a thermal boundary layer appears near the pipe end, the width of which scales as $(HR)^{-1/2}L$, where L is the half-length of the pipe. A similar boundary layer exists at the cold end. Outside the boundary layers, T_p varies linearly with a gradual slope. Thus, these regions correspond to the evaporative, adiabatic and condensing regions commonly observed in conventional heat pipes. This is the first time that the distinct regions have been captured by a single solution, without prior assumptions of their existence. If $HR \sim 1$ or less, then T_p is linear almost everywhere. This is the case found in most micro-heat-pipe

---

† Author to whom correspondence should be addressed: hwong@lsu.edu.

experiments. Our analysis of the dual-wet pipe provides an explanation for the comparatively low effective thermal conductivity in micro heat pipes, and points to ways of improving their heat transfer capabilities.

1. Introduction

A conventional heat pipe is a closed duct filled with a liquid and its vapour. The duct is usually circular in cross-section with the inner wall covered by a layer of porous material (Peterson 1994; Faghri 1995). The liquid fills the porous lining whereas the vapour fills the rest. As one end of a heat pipe is heated, the liquid evaporates and increases the vapour pressure. The higher pressure drives the vapour to the cold end, where the vapour condenses and releases the latent heat. The condensate then flows along the porous lining back to the hot end to complete the cycle. Heat pipes are efficient in transferring heat because thermal energy is carried from one end to another by evaporation, convection and condensation. Their effective thermal conductivity can be 30 times that of copper (Peterson 1994). Furthermore, there is no moving mechanical machinery in a heat pipe, resulting in low maintenance and operating costs. Consequently, heat pipes have been installed in the thermal control of, for example, the Alaska pipeline, nuclear reactor cores, and the leading edge of hypersonic aircraft (Peterson 1994; Faghri 1995).

Micro heat pipes have been developed to control the temperature of micro electronic devices (Groll *et al.* 1998; Sobhan, Rag & Peterson 2007). A micro heat pipe is a long polygonal (e.g. triangular or rectangular) capillary filled with a liquid and a long vapour bubble. The length of the bubble is comparable to that of the capillary. Figure 1 shows a vapour bubble in a square capillary under uniform temperature (Wong, Radke & Morris 1995). A cross-section reveals that the corners are occupied by liquid menisci. These channels allow liquid to flow from the cold to the hot end, functioning as the porous lining in a conventional heat pipe.

The operation of a micro heat pipe is similar to that of the conventional heat pipe. As one end of a micro heat pipe is heated, the liquid evaporates and the corner menisci recede into the corners. The higher vapour pressure at the hot end drives the vapour to the cold end where it condenses and releases the latent heat. The condensate then flows along the corner channels back to the hot end to complete the cycle. The corner flow is driven by an axial capillary-pressure gradient. A micro heat pipe can be as small as 50 μm in width, and it can be fabricated as part of an electronic circuitry. As a result, micro heat pipes are especially suited for thermal control of micro electronic devices (Groll *et al.* 1998).

The steady operation of a micro heat pipe was first modelled by Cotter (1984), who assumed liquid and vapour flows to be unidirectional. This allows the local pressure gradient to be related to the local mass flow rate. Under steady operation, the vapour and liquid mass flow rates must be equal and opposite at each point along the pipe. The vapour flow carries the latent heat and is proportional to the local heat flux (assumed known). The pressure jump across the interface is equated to the capillary pressure. This yields a differential equation for the radius of curvature of the interface in terms of the known heat flux. Solution of the equation leads to an estimate of the maximum heat flux through the pipe. The predicted maximum heat flow is more than double the values measured in experiments, and the model has been modified to yield better agreement with experiments (Longtin, Badran & Gerner 1994; Ha & Peterson

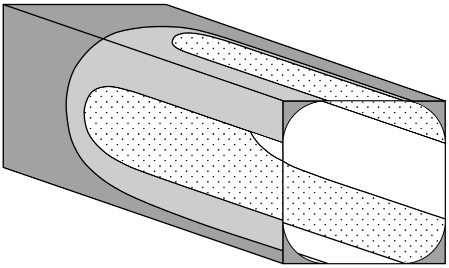

FIGURE 1. Half of a square micro heat pipe under uniform temperature. The liquid-filled corners provide a channel for liquid flow.

1998). This approach does not use the energy equation and therefore cannot describe the temperature distribution along the pipe.

Khrustalev & Faghri (1994) developed a more comprehensive model that includes the energy equation. They separated the pipe into three distinct regions (evaporator, adiabatic and condenser), and treated each region differently. In the evaporator region, they considered the meniscus near the contact line and incorporated previously published results on evaporation due to superheat and disjoining pressure (Wu & Wong 2004). In the condenser region, they assumed that a liquid film covers the wall and found the film profile based on the latent heat released by the condensate. In the adiabatic region, they imposed the condition that the liquid flow rate is constant. They then connected the three regions together by appropriate continuity conditions. Their model neglects axial heat conduction in the wall and liquid, and focuses instead on the vapour temperature. When their model is applied to the experiments by Wu & Peterson (1991), good agreement is obtained for the maximum heat flow. A similar approach is adopted by Launay, Sartre & Lallemand (2004) to calculate the effective thermal conductivity as a function of the liquid fill charge.

Suman & Kumar (2005) considered axial heat conduction in the pipe wall. They also separated the pipe into three regions, but they neglected the evaporation and condensation kinetics. Instead, the vapour flow rate is related to the heat flux, which is equated to the conductive heat flux along the pipe wall. Patching the three regions allows them to find the axial temperature distribution in the pipe. Here, we study in detail the evaporation and condensation mechanisms, and find an analytic solution for the pipe temperature that contains the three distinct regions without prior assumptions of their existence.

The effective thermal conductivity of micro heat pipes is far below that of conventional heat pipes. A typical value for the effective thermal conductivity of a conventional heat pipe is $13\,200\,\mathrm{W\,m^{-1}\,K^{-1}}$ (Peterson 1994), whereas that of a micro heat pipe is $300\,\mathrm{W\,m^{-1}\,K^{-1}}$ (Peterson, Duncan & Weichold 1993; Badran *et al.* 1997). The effective thermal conductivity of a micro heat pipe with and without a liquid differs by at most 50% (Peterson *et al.* 1993; Badran *et al.* 1997). The experimental study by Le Berre *et al.* (2003) uses a triangular micro channel with an attached side channel for liquid flow. They were able to obtain an effective thermal conductivity of $600\,\mathrm{W\,m^{-1}\,K^{-1}}$. A conventional heat pipe has three distinct temperature regions along the pipe: evaporative, adiabatic and condensing. The temperature is almost uniform in the middle adiabatic section, which is the main reason for the large effective thermal conductivity. However, this adiabatic region is missing in most micro heat pipes (Badran *et al.* 1997; Le Berre *et al.* 2003). Thus, it seems that the heat transfer capability of micro heat pipes has not been fully developed.

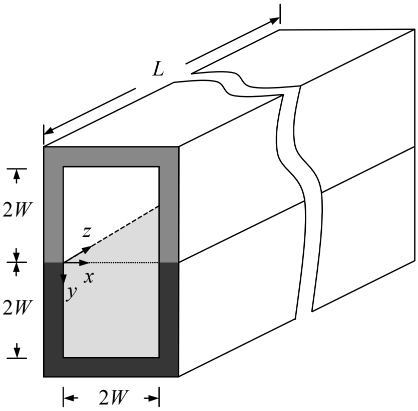

FIGURE 2. Heated half of a dual-wet heat pipe. The bottom half of the pipe is made of a wetting material and is filled by a wetting liquid, whereas the top half, which is made of a non-wetting material, is occupied by the vapour. This ensures that the contact line of the liquid-vapour interface is pinned. A coordinate system (x, y, z) is defined at the middle of the pipe with z pointing towards the hot end. The width of the pipe is $2W$.

To understand the basic heat transfer mechanisms of micro heat pipes, it is better to analyse a system without the complicated bubble geometry, but with all the essential physics retained. There are several basic elements of micro heat pipes that are required for heat transfer. The corner menisci serve as a channel for liquid flow. Thus, the new system must also contain a liquid flow channel. The liquid–vapour interfaces at the hot and cold ends change their curvatures owing to evaporation and condensation. Thus, the new system must also include a liquid–vapour interface that separates the vapour and liquid flow channels, and the interface must be able to deform under evaporation and condensation. The deformation must occur in such a way as to generate a capillary pressure difference that drives the liquid from the cold end to the hot end. Finally, the contact line has been shown to play a crucial role in evaporation and condensation and must be retained in the new system. Below, a dual-wet micro heat pipe is proposed which captures all these essential elements.

1.1. *A dual-wet micro heat pipe*

Figure 2 shows our proposed micro heat pipe, the bottom portion of which is made of a wetting material, while the top portion is a non-wetting material. The wetting portion is filled to the rim by a wetting liquid, and the non-wetting portion is filled by its vapour. This configuration ensures that the contact line of the liquid–vapour interface is pinned at the transition point between the wetting and the non-wetting wall material (Gau *et al.* 1999; Darhuber, Troian & Reisner 2001). Pinning of the interface allows a capillary-pressure gradient to drive the liquid flow. When this micro heat pipe is driven at a small temperature difference, the interface should be approximately flat, allowing the analysis to be greatly simplified. The goal of studying this dual-wet micro heat pipe is to identify key parameters that govern heat transfer.

The heat transfer mechanism of a micro heat pipe can be understood as follows. Initially, the pipe is at a uniform temperature T_0. One end of the heat pipe is then heated to temperature $T_0 + \Delta T$, and the other end cooled to $T_0 - \Delta T$. The temperature difference is maintained and the heat pipe reaches a steady state. At the hot end, the equilibrium vapour pressure is higher than that at the cold end, and the vapour-pressure gradient drives a vapour flow. Because the vapour moves away from the hot end, the vapour pressure at the hot end drops below the equilibrium value, and this pressure drop induces continuous evaporation. At the cold end, the vapour pressure is higher than the local equilibrium vapour pressure, leading to condensation. The condensate increases the liquid volume at the cold end and raises the liquid–vapour interface, whereas the interface sags at the hot end owing to evaporation. Because the contact lines are pinned, the interfacial profile creates a capillary pressure gradient in the liquid along the pipe, which drives the liquid from the cold to the hot end. In general, $\Delta T \ll T_0$, and the vapour and liquid flows and the temperature distribution along the pipe are skew-symmetric about the midpoint of the pipe. Thus, only the heated half of the pipe is studied (figure 2).

Flow fields inside a micro heat pipe vary slowly in the axial direction because of the high aspect ratio of the pipe. Hence, at each cross-sectional plane, the evaporative motion can be taken as two-dimensional. This in-plane motion is studied first; the governing equations are given in § 2 and are made dimensionless in § 3. Two dimensionless parameters emerge: an evaporation number E ($\gg 1$) and a Marangoni number M ($\gg 1$). The evaporation number E measures the ratio of the evaporative heat flux at the interface to the conductive heat flux in the liquid, if both are driven by the same temperature difference. The temperature field in the cross-sectional plane depends on E only, and is solved in the limit $E \to \infty$ in § 4. The temperature field has a singular region near the contact line and is resolved by the method of matched asymptotic expansions. This leads to an analytical expression for the interfacial temperature, which is used to find the evaporation rate Q in the cross-sectional plane in § 5. The liquid flow in the cross-sectional plane does not affect the evaporation rate and is presented in the Appendix.

Sections 6 to 10 use Q to find the temperature distribution and vapour and liquid flows along the pipe. The heat rate q is constant along the pipe because the pipe is insulated at the outer wall. Inside the pipe, heat is transferred by vapour flow and by conduction in the liquid and wall, and the sum is equal to q, as shown in § 6. The two modes of heat transfer are coupled by the local evaporation rate Q found in § 5. The evaporation rate Q depends on the local vapour pressure p_g and pipe temperature T_p. This is a unique feature of our model, and it leads to a thermal boundary layer near the pipe end.

The pipe temperature T_p is solved in § 7. The analytic solution depends on three dimensionless numbers: H, R and the aspect ratio S ($=W/L$) of the pipe. The Heat-pipe number H is the ratio of heat transfer by vapour flow to that by conduction in the pipe wall and liquid, whereas R is the ratio of viscous resistance of vapour flow to interfacial evaporation resistance for the same pressure gradient and volume flow rate. If $HR \gg 1$, a thermal boundary layer appears near the pipe end in which the temperature varies rapidly. The width of the layer scales as $(HR)^{-1/2}L$, where L is half the pipe length. Outside the boundary layer, the temperature varies linearly with a small slope. Thus, these regions correspond to the evaporative, adiabatic and condensing regions commonly observed in heat pipes. This is the first time that the distinct regions are captured by a single temperature distribution, without prior assumptions of their existence. If $HR \sim 1$ or less, then the temperature field is almost linear. This is the case found in most micro-heat-pipe experiments. Our analysis of the dual-wet micro heat pipe provides an explanation for the lack of three distinct regions, and for the comparatively low effective thermal conductivity in micro heat pipes.

The constant heat rate q through the pipe is also determined in § 7. The conductive heat rate q_c is used to make q dimensionless and this yields a Nusselt number $Nu = q/q_c$. We find that as $H \to \infty$, $Nu \sim H$, and as $H \to 0$, $Nu \to 1$.

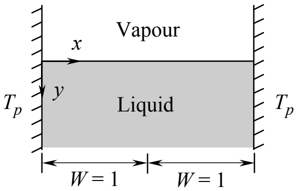

FIGURE 3. A cross-section of the dual-wet heat pipe. Cartesian coordinates (x, y) are defined with the origin at the contact line on the left-hand wall. The walls are separated by $2W$ and held at temperature T_p. The vapour pressure drops below the equilibrium value to induce continuous evaporation. Liquid is supplied at the bottom to keep the interface stationary.

The vapour pressure p_g is found in § 8 and it varies almost linearly along the pipe, independent of H. The vapour volume flow rate, however, shows a boundary-layer structure near the pipe end as $H \to \infty$ (§ 9). The liquid flow rate can be determined from the vapour flow rate by an integral mass balance (§ 10). This in turn yields the liquid pressure gradient assuming that the liquid flow is unidirectional. The liquid and vapour pressure difference then gives the curvature of the interface (§ 11). We discuss the assumptions and implications of this work in § 12 and conclude in § 13.

2. Evaporation in a cross-sectional plane

The cross-section is shown in figure 3. The cavity is bounded by two vertical walls separated by a distance $2W$. The bottom half of the cavity is filled with a liquid and the top half by its vapour. The walls are made of a wetting material at the bottom, and a non-wetting material at the top, and both are maintained at temperature T_p. Initially, the system is in equilibrium, so that the liquid and vapour are at temperature T_p, and the vapour is at the corresponding equilibrium pressure p_e. There is no motion in either the vapour or the liquid, and the interface is taken to be flat. The vapour pressure is subsequently reduced to $p_g < p_e$ and maintained at that level. This drop in vapour pressure induces continuous evaporation at the interface. (This pressure drop is caused by vapour flow along the pipe.) Since we are interested in the steady-state performance of micro heat pipes, only time-independent equations are required for liquid flow and heat conduction in the liquid:

$$\nabla p_f = \mu_f \nabla^2 \boldsymbol{u}, \tag{2.1}$$

$$\nabla \cdot \boldsymbol{u} = 0, \tag{2.2}$$

$$\nabla^2 T = 0, \tag{2.3}$$

where p_f is liquid pressure, μ_f is liquid viscosity, $\boldsymbol{u} = u\boldsymbol{i} + v\boldsymbol{j}$ is liquid velocity, and T is liquid temperature. A Cartesian coordinate system (x, y) is defined as shown in figure 3, and $\nabla = \boldsymbol{i}\partial/\partial x + \boldsymbol{j}\partial/\partial y$. Owing to the small size of micro heat pipes, convective heat transfer, inertia and gravity are negligible, as detailed in § 12. The vapour exerts insignificant shear stress on the liquid, and has much lower thermal conductivity than that of the liquid. Thus, the vapour has negligible effect on the liquid motion and heat conduction. Consequently, the vapour pressure p_g is taken to be constant and is the only parameter considered in the vapour region.

On the wall at $x = 0$, we apply the no-slip boundary condition:

$$u = 0, \quad v = 0, \tag{2.4}$$

and impose a prescribed constant temperature,

$$T = T_p. \tag{2.5}$$

Owing to symmetry, only half of the cross-sectional domain need be analysed. At the symmetry plane $x = W$,

$$\frac{\partial v}{\partial x} = 0, \quad u = 0, \quad \frac{\partial T}{\partial x} = 0. \tag{2.6}$$

The interface is pinned at the walls between the wetting and non-wetting parts, and liquid is replenished at the bottom to balance the loss by evaporation. The interface is taken as flat because surface tension dominates in micro heat pipes owing to the small size. Thus, the interface is located at $y = 0$ (figure 3). At the interface, the vertical velocity v is non-zero owing to evaporation:

$$m = -\rho_f v, \tag{2.7}$$

where ρ_f is the liquid density and m is the local evaporative mass flux (m is positive for evaporation and negative for condensation). The evaporation rate in half of the domain is

$$Q = \int_0^W v \, \mathrm{d}x. \tag{2.8}$$

The main purpose of the two-dimensional analysis in the cross-sectional plane is to find Q. At the interface, the evaporative heat flux is supplied by the conductive heat flux in the liquid:

$$m h_{fg} = k_f \frac{\partial T}{\partial y}. \tag{2.9}$$

Here, h_{fg} is the latent heat of evaporation, and k_f is the liquid thermal conductivity. The interfacial shear stress in the liquid balances a surface tension gradient:

$$\mu_f \frac{\partial u}{\partial y} = -\frac{\mathrm{d}\sigma}{\mathrm{d}x} = -\frac{\mathrm{d}\sigma}{\mathrm{d}T}\frac{\mathrm{d}T}{\mathrm{d}x}, \tag{2.10}$$

where σ is the surface tension, which varies along the interface because the temperature varies. In this work, $\mathrm{d}\sigma/\mathrm{d}T$ is assumed constant owing to the small variation in temperature. The normal stress balance does not enter at this stage since the interface is taken as flat.

The evaporative mass flux is assumed to be proportional to the drop in vapour pressure from the equilibrium value (Plesset & Prosperetti 1976; Wayner 1993; Ajaev & Homsy 2006):

$$m = c(p_i - p_g), \quad c = \frac{\alpha}{(2\pi R_s T_p)^{1/2}}, \tag{2.11}$$

where p_i is the equilibrium vapour pressure at the local interfacial temperature $T_i = T_i(x)$, α is the accommodation coefficient, and R_s is the specific gas constant. The parameter c is proportional to the inverse of the sound speed in vapour. The flux equation (2.11), derived by a kinetic theory, conserves momentum and energy at the interface, whereas some other commonly used forms do not (Barrett & Clement 1992). We can express p_i in terms of T_i. Since p_i is only a function of the interfacial temperature T_i and p_i is close to p_g, by Taylor's expansion,

$$p_i = p_g + \frac{\mathrm{d}p_i}{\mathrm{d}T_i}(T_i - T_g) \tag{2.12}$$

where T_g is the liquid–vapour equilibrium temperature at pressure p_g. The gradient $\mathrm{d}p_i/\mathrm{d}T_i$ can be evaluated using the Clapeyron relation because $p_i = p_i(T_i)$ is a thermodynamic relation (Carey 1992):

$$\frac{\mathrm{d}p_i}{\mathrm{d}T_i} = \frac{\rho_e h_{fg}}{T_p}, \tag{2.13}$$

where ρ_e is the equilibrium vapour density at temperature T_p. Although the gradient should be evaluated at temperature T_g, we use T_p because it is a boundary condition and because $|T_p - T_g| \ll T_p$ and only the linear term in temperature is kept in (2.12). Substitution of p_i in (2.12) into (2.11) yields

$$m = \frac{c\rho_e h_{fg}(T_i - T_g)}{T_p}, \tag{2.14}$$

therefore, the evaporative mass flux $m = m(T_i)$. This equation is similar to that used by Burelbach, Bankoff & Davis (1988).

Far below the pinned interface, the liquid flow is non-zero owing to evaporation and the temperature approaches the wall temperature. Thus, as $y \to \infty$,

$$\int_0^W v\,\mathrm{d}x \to -Q, \quad u \to 0, \quad T \to T_p. \tag{2.15}$$

Here, we have modified the liquid domain so that the bottom wall is extended to infinity. This modification allows a simple analytic solution for the temperature field and has a negligible effect on the evaporation rate Q, as shown in § 5 (see also § 12).

3. Dimensionless equations governing evaporation

Since the liquid motion is induced by evaporation, the surface evaporative flux equation (2.7), (2.11) and (2.14) are used to yield a velocity scale:

$$U = \frac{c}{\rho_f}(p_e - p_g) = \frac{c\rho_e h_{fg}(T_p - T_g)}{\rho_f T_p}. \tag{3.1}$$

A set of dimensionless variables is defined:

$$x^* = \frac{x}{W}, \quad y^* = \frac{y}{W}, \quad u^* = \frac{u}{U}, \quad p_f^* = \frac{p_f W}{\mu_f U}, \quad T^* = \frac{T - T_g}{T_p - T_g}, \quad Q^* = \frac{Q}{UW}. \tag{3.2}$$

The governing equations become

$$\nabla^* p_f^* = \nabla^{*2} \boldsymbol{u}^*, \tag{3.3}$$

$$\nabla^* \cdot \boldsymbol{u}^* = 0, \tag{3.4}$$

$$\nabla^{*2} T^* = 0, \tag{3.5}$$

where $\nabla^* = \boldsymbol{i}\,\partial/\partial x^* + \boldsymbol{j}\,\partial/\partial y^*$. At the wall $x^* = 0$,

$$u^* = 0, \quad v^* = 0, \quad T^* = 1. \tag{3.6}$$

At the symmetric plane $x^* = 1$,

$$\frac{\partial v^*}{\partial x^*} = 0, \quad u^* = 0, \quad \frac{\partial T^*}{\partial x^*} = 0. \tag{3.7}$$

At the interface $y^* = 0$,

$$v^* = -T^*, \quad \frac{\partial u^*}{\partial y^*} = M\frac{\partial T^*}{\partial x^*}, \quad ET^* = \frac{\mathrm{d}T^*}{\mathrm{d}y^*}, \tag{3.8}$$

in which

$$M = -\frac{\rho_f T_p}{c\rho_e h_{fg}\mu_f}\frac{\mathrm{d}\sigma}{\mathrm{d}T}, \quad E = \frac{cW\rho_e h_{fg}^2}{k_f T_p}. \tag{3.9}$$

Here, M is the Marangoni number, which measures the ratio of the surface tension gradient induced by temperature variation to the viscous shear stress caused by evaporation at the interface (Levich 1962). We define an evaporation number E that reflects the ratio of the evaporative heat flux at the interface to the conductive heat flux in the liquid, assuming that both are driven by the same temperature difference. It identifies a length scale ($E^{-1}W$) over which the conductive heat flux becomes comparable to the evaporative heat flux under the same temperature difference. The evaporation number E is the inverse of the non-equilibrium parameter defined by Burelbach *et al.* (1988). For a silicon micro heat pipe 45 μm wide charged with methanol at 42 °C, $M = 40.8$ and $E = 780$ (Peterson *et al.* 1993). (The parameters are given in table 1)

Far from the liquid interface as $y^* \to \infty$,

$$\int_0^1 v^*\,\mathrm{d}x^* \to -Q^*, \quad u^* \to 0, \quad T^* \to 1. \tag{3.10}$$

The dimensionless evaporation rate in half the domain is found from the vertical liquid velocity at the interface:

$$Q^* = -\int_0^1 v^*\,\mathrm{d}x^*. \tag{3.11}$$

Since $v^* = -T^*$ at the interface as specified by (3.8),

$$Q^* = \int_0^1 T^*\,\mathrm{d}x^*. \tag{3.12}$$

Thus, to find Q^*, we need only to focus on the interfacial temperature.

The above fluid flow and heat transfer problem contains two dimensionless parameters: $E(\gg 1)$ and $M(\gg 1)$. The temperature field depends only on E. The velocity field is coupled to the temperature field through the boundary conditions, in which M appears. Since the objective of the two-dimensional analysis is to find Q^*, which depends only on the interfacial temperature, we will focus below on the temperature field and present the velocity solution in the Appendix.

4. Temperature field in the cross-sectional plane

The temperature field is expanded in the limit $E \to \infty$ as

$$T^* = t_0 + E^{-1}t_1 + \cdots. \tag{4.1}$$

A boundary layer exists near the wall. This is shown by a discontinuity in the leading-order temperature field t_0. To see the discontinuity, T^* in (4.1) is substituted into (3.6) to yield $t_0 = 1$ at the wall $x^* = 0$. However, substitution of T^* in (4.1) into (3.8) leads to $t_0 = 0$ at $y^* = 0$. This jump in temperature at the contact line appears often in evaporation problems and leads to unbounded temperature gradients. In the present problem, this jump results from the disappearance of the derivative in (3.8) because it is multiplied by E^{-1}. This hints at the existence of an inner region. An inner problem is formulated next which shows that the temperature T^* decays smoothly along the interface from $T^* = 1$ at the wall to $T^* = 0$ away from the wall in a distance scaled by

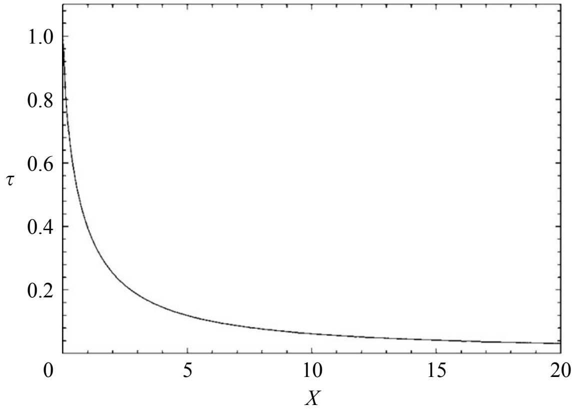

FIGURE 4. Dimensionless temperature τ along the liquid–vapour interface in the inner region as given by (4.4).

E^{-1}. The existence of the inner problem results from the constitutive equation (2.14) for the evaporative mass flux, and from the constant temperature condition at the wall.

4.1. *Inner temperature* τ

A set of inner variables is defined as

$$X = Ex^*, \; Y = Ey^*, \; \tau(X, Y) = T^*(x^*, y^*). \tag{4.2}$$

The inner temperature field obeys

$$\nabla^2 \tau = 0. \tag{4.3a}$$

At the wall $X = 0$,

$$\tau = 1. \tag{4.3b}$$

At the liquid–vapour interface Y = 0,

$$\tau = \frac{\partial \tau}{\partial Y}. \tag{4.3c}$$

As $X \to \infty$,

$$\tau \to 0. \tag{4.3d}$$

Since the parameter E is scaled out of the problem, this inner solution holds for all orders of E. Thus, the inner problem describes the local behaviour near the contact line. It is intrinsic to the evaporation problem, and is independent of the outer problem.

To solve (4.3), a new dependent variable is defined: $G = \partial \tau/\partial Y - \tau$ (Morris 2000). The governing equation remains the same, $\nabla^2 G = 0$, but the boundary condition at the liquid–vapour interface $Y = 0$ is reduced to $G = 0$, and that at the wall $X = 0$, $G = -1$. This leads to a simple solution: $G = (2/\pi)\tan^{-1}(X/Y) - 1$. Thus, the inner temperature obeys $\partial \tau/\partial Y - \tau = (2/\pi)\tan^{-1}(X/Y) - 1$, the solution of which is

$$\tau = 1 - \frac{2}{\pi}\tan^{-1}\left(\frac{X}{Y}\right) + \frac{2}{\pi}\mathrm{e}^{Y} X \int_{Y}^{\infty} \frac{\mathrm{e}^{-\lambda}}{\lambda^2 + X^2}\,\mathrm{d}\lambda. \tag{4.4}$$

The temperature distribution along the liquid–vapour interface is plotted in figure 4. It indicates that the temperature varies smoothly from 1 at the wall to 0 away from the wall. This solution agrees with that of Morris (2000) who considered a more general problem in which the isothermal condition is not imposed at the solid–liquid interface, but at the outer wall of the solid. Also, in his problem, the liquid–vapour interface need not be perpendicular to the wall. These additional complexities only change the total evaporation rate by a factor that is less than or equal to one.

4.2. *Zero-order outer temperature* t_0

According to the expansion in (4.1), the zero-order outer temperature satisfies

$$\nabla^2 t_0 = 0. \tag{4.5a}$$

At the wall $x^* = 0$,

$$t_0 = 1, \tag{4.5b}$$

while on the symmetric plane $x^* = 1$,

$$\frac{\partial t_0}{\partial x^*} = 0. \tag{4.5c}$$

At the liquid–vapour interface $y^* = 0$,

$$t_0 = 0. \tag{4.5d}$$

Far from the interface as $y^* \to \infty$,

$$t_0 \to 1. \tag{4.5e}$$

An analytical solution of (4.5) obtained by conformal mapping is given by Churchill & Brown (1984):

$$t_0 = 1 - \frac{2}{\pi}\tan^{-1}\left[\frac{\sin(\pi x^*/2)}{\sinh(\pi y^*/2)}\right]. \tag{4.6}$$

4.3. *First-order outer temperature* t_1

The evaporation rate Q^* depends on the interfacial temperature according to (3.12). The outer solution (4.6) shows that $t_0 = 0$ at the interface $y^* = 0$, which means that t_0 does not contribute to the evaporation rate. Thus, we must find t_1, but only at the interface. This can be done simply by substitution of the temperature expansion in (4.1) into (3.8): at the interface $y^* = 0$,

$$t_1 = \frac{\partial t_0}{\partial y^*} = \operatorname{cosec}\left(\frac{\pi x^*}{2}\right). \tag{4.7}$$

This is all we need to calculate the evaporative rate Q^*.

5. Evaporation rate per contact-line length

The dimensionless evaporation rate Q^* depends on the interfacial temperature according to (3.12):

$$Q^* = \int_0^1 T^*\, \mathrm{d}x^*. \tag{5.1}$$

The temperature field has an inner and outer structure. At the liquid–vapour interface $y^* = 0$, the inner temperature field in (4.4) reduces to

$$\tau = \frac{2X}{\pi}\int_0^\infty \frac{\mathrm{e}^{-\lambda}}{\lambda^2 + X^2}\,\mathrm{d}\lambda. \tag{5.2}$$

Integration by parts yields

$$\tau = \frac{2}{\pi X}\left[1 + \frac{2}{X^2}\int_0^\infty \frac{\lambda \mathrm{e}^{-\lambda}}{[1+(\lambda/X)^2]^2}\,\mathrm{d}\lambda\right]. \tag{5.3}$$

As $X \to \infty$,

$$\tau \to \frac{2}{\pi X} + \cdots. \tag{5.4}$$

The first-order outer temperature field at the liquid-vapour interface is given in (4.7) as

$$t_1 = \operatorname{cosec}\left(\frac{\pi x^*}{2}\right). \tag{5.5}$$

As $x^* \to 0$,

$$t_1 \to \frac{2}{\pi x^*} + \cdots. \tag{5.6}$$

Therefore, the composite solution of the interfacial temperature is

$$T^* = \frac{2Ex^*}{\pi}\int_0^\infty \frac{\mathrm{e}^{-\lambda}}{\lambda^2 + E^2 x^{*2}}\,\mathrm{d}\lambda + E^{-1}\operatorname{cosec}\left(\frac{\pi x^*}{2}\right) - \frac{2E^{-1}}{\pi x^*}. \tag{5.7}$$

The first term on the right-hand side comes from the inner region, the second term from the outer region, and the last term from the matching region.

The evaporation rate Q^* in (5.1) is found in the limit $E \to \infty$. The first term in (5.7) comes from the inner region; its contribution to the evaporation rate is

$$Q_1 = \frac{2E}{\pi x^*}\left(\int_0^\infty \mathrm{e}^{-\lambda}\int_0^1 \frac{x^*}{\lambda^2 + E^2 x^{*2}}\,\mathrm{d}x^*\,\mathrm{d}\lambda\right), \tag{5.8}$$

which simplifies to

$$Q_1 = \frac{2}{\pi}E^{-1}\ln E + \frac{2}{\pi\gamma}E^{-1} + \frac{E^{-1}}{\pi}\int_0^\infty \mathrm{e}^{-\lambda}\ln(1 + E^{-2}\lambda^2)\,\mathrm{d}\lambda, \tag{5.9}$$

where $\gamma \approx 0.57722\ldots$ is the Euler number. The last term in the above equation is of order E^{-3}. Thus, to leading orders,

$$Q_1 = \frac{2E^{-1}}{\pi}(\ln E + \gamma). \tag{5.10}$$

The second and third terms in (5.7) come from the outer and matching regions. Their contributions to the evaporation rate can be calculated exactly. Thus, the evaporation rate in half of the cross-sectional plane is

$$Q^* = \frac{2E^{-1}}{\pi}\left[\ln E + \gamma + \ln\left(\frac{4}{\pi}\right)\right]. \tag{5.11}$$

The evaporation rate in the inner region dominates. For example, if $E = 10^3$, about 97% of Q^* comes from the inner region.

In the derivation of the temperature field, the liquid domain is modified to allow a simple analytic solution in the outer region. Equation (5.11) shows that the effect of that modification is second order in Q^*. To leading order,

$$Q^* = \frac{2}{\pi}E^{-1}\ln E. \tag{5.12}$$

This comes only from the inner region. Since the inner solution is not influenced by the outer problem, (5.12) is independent of the liquid domain height.

6. Fluid flow and heat transfer along the pipe

Figure 2 shows the heated half of the dual-wet micro heat pipe, which is a rectangular cavity of dimensions $2W \times 4W \times L$ surrounded by a wall made of two different materials. In the previous sections, we found the evaporation rate Q at a cross-sectional plane of the pipe. We find that the in-plane evaporation occurs mainly in the corner region near the contact line. The dimensional liquid volume evaporation rate per unit contact-line length is

$$Q = \frac{c(p_e - p_g)W}{\rho_f} Q^*(E), \tag{6.1}$$

where $Q^*(E)$ is given in (5.11) or (5.12). The purpose of the following sections is to calculate the vapour and liquid flows along the pipe induced by Q and the resulting temperature distribution.

The expression of Q in (6.1) shows that the evaporation is driven by the difference $(p_e - p_g)$, where p_e is the equilibrium vapour pressure and p_g is the vapour pressure, both varying along the pipe. The equilibrium vapour pressure p_e depends only on the local liquid (or wall) temperature T_p, and this dependence can be made explicit by expanding around the initial temperature T_0, which is also the temperature at the mid-point of the pipe owing to symmetry. By the Clapeyron relation (Carey 1992),

$$p_e = P_0 + \frac{\mathrm{d}p_e}{\mathrm{d}T_p}(T_p - T_0), \quad \frac{\mathrm{d}p_e}{\mathrm{d}T_p} = \frac{\rho_0 h_{fg}}{T_0}, \tag{6.2}$$

where P_0 and ρ_0 are, respectively, the equilibrium vapour pressure and density at T_0, and their values are known. Thus, Q becomes

$$Q = \frac{cWQ^*(E)}{\rho_f}\left[\frac{\mathrm{d}p_e}{\mathrm{d}T_p}(T_p - T_0) - (p_g - P_0)\right], \tag{6.3a}$$

$$c = \frac{\alpha}{(2\pi R_s T_0)^{1/2}}, \tag{6.3b}$$

$$E = \frac{cW\rho_0 h_{fg}^2}{k_f T_0}. \tag{6.3c}$$

Since $T_p \approx T_0$ and $p_g \approx P_0$, only linear terms in $(T_p - T_0)$ and $(p_g - P_0)$ are kept in Q, and only the reference parameters T_0 and ρ_0 are left in c and E (see (2.11) and (3.9) for their original definitions). Equation (6.3) shows that the evaporation rate Q rises if the pipe temperature T_p increases or if the vapour pressure p_g decreases. Near the hot end, the liquid evaporates into vapour ($Q > 0$), which flows to the cold end and condenses into liquid ($Q < 0$) to release the latent heat. At the middle of the pipe, $T_p = T_0$ and $p_g = P_0$, so that $Q = 0$. Since $Q > 0$ in the heated half of the pipe, the temperature term in (6.3*a*) is always larger than the pressure term, even though both terms are positive.

Fluid flow along the pipe is taken as unidirectional because the pipe is slender. Thus, the vapour pressure gradient varies linearly with the local vapour flow rate (White 2006):

$$\frac{\mathrm{d}p_g}{\mathrm{d}z} = -\frac{\mu_g V_g}{C_g W^4}, \tag{6.4}$$

where μ_g is the vapour viscosity, V_g is the vapour volume flow rate in the z-direction, and C_g is a constant that depends on the cross-sectional shape. For a square flow domain of width $2W$, $C_g = 0.5623$ (White 2006). The volume flow rate varies along the pipe owing to evaporation. A local mass balance specifies

$$\frac{\mathrm{d}V_g}{\mathrm{d}z} = \frac{2\rho_f Q}{\rho_0}. \tag{6.5}$$

The factor 2 is required because there are two contact lines at each cross-sectional plane. If we scale $z \sim L$, then $V_g \sim 2\rho_f QL/\rho_0$, so that the pressure gradient in (6.4) is

$$\frac{\mathrm{d}p_g}{\mathrm{d}z} \sim \frac{2\mu_g \rho_f L}{C_g W^4 \rho_0} Q. \tag{6.6}$$

From the evaporation rate equation in (6.3), we can derive another relation between the pressure gradient and Q:

$$\frac{\mathrm{d}p_g}{\mathrm{d}z} \sim \frac{\rho_f}{cWLQ^*(E)} Q. \tag{6.7}$$

Thus, the ratio of viscous resistance of vapour flow to interfacial evaporation resistance is

$$R = \frac{2\mu_g c Q^*(E)}{C_g W \rho_0} \left(\frac{L}{W}\right)^2. \tag{6.8}$$

If the viscous resistance dominates, $R \gg 1$; if the evaporation resistance dominates, $R \ll 1$. This dimensionless number plays an important role in later sections.

Heat conduction along the heat pipe is taken to be one dimensional. The pipe is insulated outside, and at each point along the pipe the liquid temperature is assumed to be the same as the wall temperature T_p. This liquid-wall system loses heat by evaporation. An energy balance on this system gives

$$(A_w k_w + A_f k_f)\frac{\mathrm{d}^2 T_p}{\mathrm{d}z^2} - 2\rho_f h_{fg} Q = 0, \tag{6.9}$$

where A is the cross-sectional area and k is the thermal conductivity with its subscript indicating either wall (w) or liquid (f). The vapour phase has a much lower thermal conductivity and does not contribute to heat conduction. Equation (6.9) can be integrated once after Q has been replaced using (6.5):

$$(A_w k_w + A_f k_f)\frac{\mathrm{d}T_p}{\mathrm{d}z} - \rho_0 h_{fg} V_g = q. \tag{6.10}$$

The integration constant q is the heat rate along the pipe from the hot end towards the cold. This heat rate is constant because the pipe is insulated. The first term in (6.10) is the conduction heat rate in the liquid and wall, and the second term is the heat rate carried by the vapour flow. This equation shows the heat transfer physics in a micro heat pipe.

Equation (6.10) can be integrated again with V_g substituted using (6.4):

$$(A_w k_w + A_f k_f)(T_p - T_0) + \frac{\rho_0 h_{fg} C_g W^4}{\mu_g}(p_g - P_0) = qz, \tag{6.11}$$

where the boundary conditions at $z = 0$ have been imposed. This equation gives the vapour pressure p_g in terms of the pipe temperature T_p. Thus, the two dependent variables can be solved separately.

An important dimensionless number emerges from (6.11). Since (6.11) contains heat rate by conduction (first term) and by vapour flow (second term), a ratio can be defined as

$$H \sim \frac{(\rho_0 h_{fg} C_g W^4/\mu_g)(p_g - P_0)}{(A_w k_w + A_f k_f)(T_p - T_0)}. \tag{6.12}$$

A measure of $(p_g - P_0)/(T_p - T_0)$ is $\mathrm{d}p_e/\mathrm{d}T_p$, which is the value that gives zero Q in (6.3a). Since $\mathrm{d}p_e/\mathrm{d}T_p = \rho_0 h_{fg}/T_0$ according to (6.2), we obtain

$$H = \frac{\rho_0^2 h_{fg}^2 C_g W^4}{(A_w k_w + A_f k_f)\mu_g T_0}. \tag{6.13}$$

This heat-pipe number represents the ratio of vapour-flow heat rate to conduction heat rate. If vapour flow dominates, $H \gg 1$, and if conduction dominates, $H \ll 1$.

7. Liquid and wall temperature T_p along the pipe

The pipe temperature T_p obeys (6.9), which contains $Q = Q(T_p, p_g)$. Since p_g is related to T_p by (6.11), (6.9) becomes

$$\frac{\mathrm{d}^2 T_p}{\mathrm{d}z^2} - \frac{R}{L^2}\left[(1+H)\left(T_p - T_0\right) - \frac{qz}{A_w k_w + A_f k_f}\right] = 0. \tag{7.1}$$

Solution of this equation with the boundary conditions that $T_p = T_0$ at $z = 0$ and $T_p = T_h = T_0 + \Delta T$ at $z = L$ yields

$$\frac{T_p - T_0}{T_h - T_0} = \left[1 - \left(\frac{1}{1+H}\right)\frac{q}{q_c}\right]\frac{\sinh\left[(1+H)^{1/2} R^{1/2} z/L\right]}{\sinh\left[(1+H)^{1/2} R^{1/2}\right]} + \left(\frac{1}{1+H}\right)\left(\frac{q}{q_c}\right)\frac{z}{L}, \tag{7.2a}$$

where

$$q_c = \frac{(A_w k_w + A_f k_f)(T_h - T_0)}{L}, \tag{7.2b}$$

is the conductive heat rate in the liquid and wall. The dimensionless parameters R and H are defined in (6.8) and (6.13).

The heat rate q along the pipe is still unknownin (7.2a), and can be found by imposing a boundary condition. At the end of the pipe, the liquid–vapour interface meets the end wall at a contact line of length $2W$ (figure. 2). Evaporation at this contact line gives a non-zero vapour flow rate at the end of the pipe. Thus, at $z = L$

$$V_g = -2WQ\frac{\rho_f}{\rho_0}. \tag{7.3}$$

Therefore, q can be found from (6.10) and (7.2) as

$$\frac{q}{q_c} = Nu = (1+H)\frac{(1+H)^{1/2}R^{1/2}\coth\left[(1+H)^{1/2} R^{1/2}\right] + (1+H)RS}{H + (1+H)^{1/2}R^{1/2}\coth\left[(1+H)^{1/2} R^{1/2}\right] + (1+H)RS}, \tag{7.4}$$

where a Nusselt number has been defined as the ratio of total heat rate to conductive heat rate. The ratio depends on three dimensionless parameters: the heat-pipe number H, the ratio of viscous to evaporative resistance R, and the aspect ratio of the heat pipe $S (= W/L)$. As $H \to 0$,

$$Nu \to 1 + \left[1 - \frac{1}{R^{1/2}\coth\left(R^{1/2}\right) + RS}\right] H + \cdots. \tag{7.5a}$$

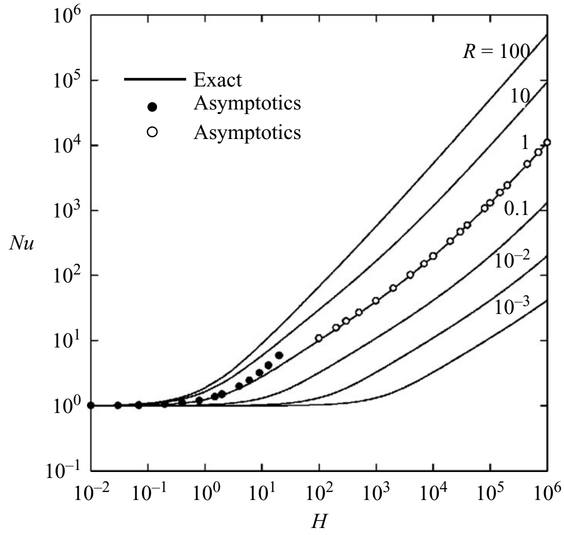

FIGURE 5. The Nusselt number Nu along the pipe versus the heat-pipe number H for $S=0.01$ and various R. The exact solution (—) and its asymptotic expansions (symbols) are given in (7.4) and (7.5). The asymptotic solutions are calculated for $R=1$.

which approaches unity as expected. As $H \to \infty$,

$$Nu \to \left(\frac{RS}{1+RS}\right)H + \left[\frac{R^{1/2}}{(1+RS)^2}\right]H^{1/2} + \cdots . \qquad (7.5b)$$

Thus, for enhanced heat transfer, we should design a heat pipe such that $H \gg 1$ and $RS \sim 1$ or greater. In figure 5, we plot Nu versus H for $S=10^{-2}$ and various R. It shows that $Nu \gg 1$ for $HR \gg 1$, and $Nu \sim 1$ for $HR \sim 1$ or less. Figure 5 also shows that Nu increases linearly with H as $H \to \infty$, and its value at a fixed H increases with R.

The pipe temperature T_p is found by substituting q/q_c in (7.4) into (7.2a). The normalized temperature $(T_p - T_0)/(T_h - T_0)$ depends on H, R and S. In the limit $H \to 0$,

$$\frac{T_p - T_0}{T_h - T_0} \to \frac{z}{L} + \left[\frac{\sinh\left(R^{1/2}z/L\right)}{\sinh\left(R^{1/2}\right)} - \frac{z}{L}\right]\frac{H}{R^{1/2}\coth\left(R^{1/2}\right) + RS} + \cdots . \qquad (7.6a)$$

Thus, when conduction dominates, T_p increases linearly along the pipe as expected. When vapour flow dominates, $H \gg 1$, and

$$\begin{aligned}\frac{T_p - T_0}{T_h - T_0} \to {} & \frac{RS}{1+RS}\left[1 + \frac{1}{S(1+RS)(HR)^{1/2}}\right]\left(\frac{z}{L}\right) \\ & + \frac{1}{1+RS}\left\{1 - \left[\frac{R^{1/2}}{2}\left(1-\frac{z}{L}\right) - \frac{1}{1+RS}\right]H^{-1/2}\right\} \\ & \times \exp\left[-(HR)^{1/2}(1-z/L)\right] + O(H^{-1}). \qquad (7.6b)\end{aligned}$$

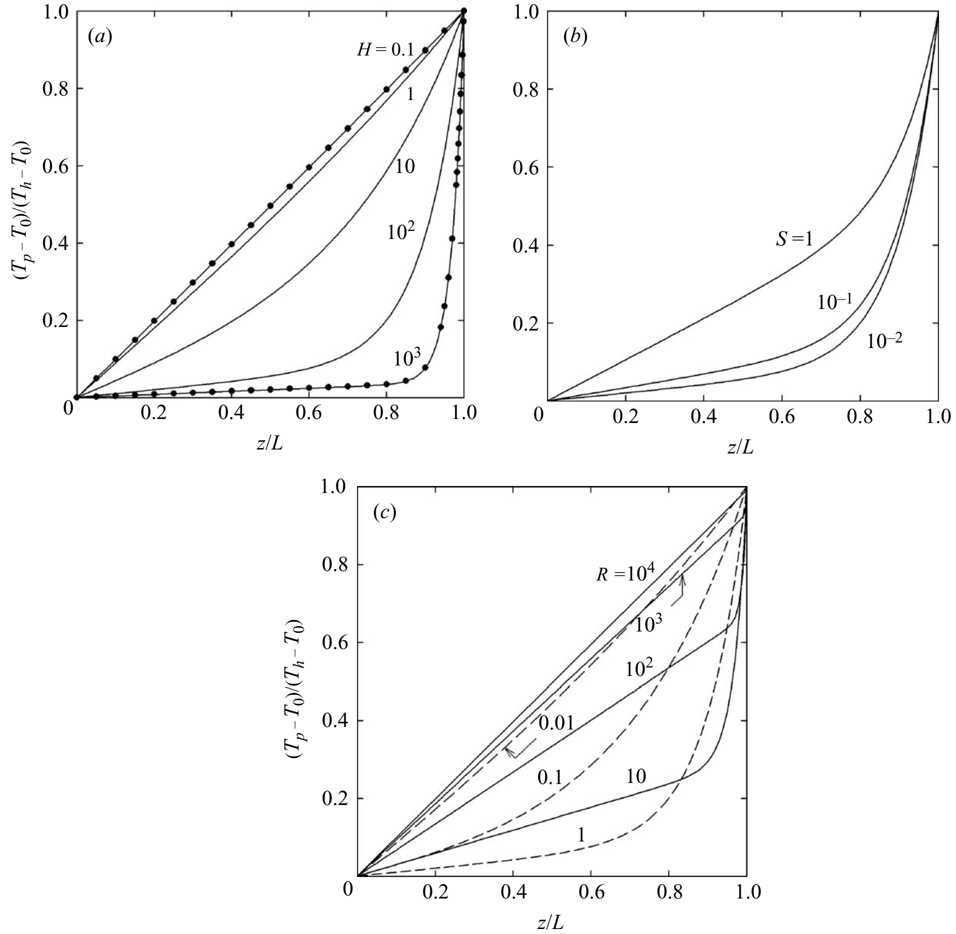

FIGURE 6. Normalized temperature along the pipe. (*a*) $R = 1$, $S = 0.01$ and H varies from 0.1 to 10^3. The exact solution (—) and its asymptotic expansions (symbols) are given in (7.2) and (7.6). (*b*) $R = 1$, $H = 100$ and various $S \leqslant 1$. Temperature profiles for $S < 10^{-2}$ are close to that for $S = 10^{-2}$. (*c*) $H = 100$, $S = 0.01$ and various R.

The leading two terms of the asymptotic expansion reveal the existence of a boundary layer at the pipe end. The width of the boundary layer scales as

$$\delta z \sim \frac{L}{(HR)^{1/2}}. \tag{7.7}$$

Outside the boundary layer, $L - z \gg \delta z$ and only the first term remains on the right-hand side of (7.6*b*). This term describes the behaviour of T_p in the outer region: T_p increases linearly along the pipe with a slope that decreases with increasing H. Inside the boundary layer, T_p rises rapidly to T_h at $z = L$. Figure 6(*a*) shows the normalized temperature along the pipe calculated using (7.2*a*) and (7.4) for $R = 1$, $S = 0.01$ and $H = 0.1$, 1, 10, 10^2 and 10^3. It shows that when $H \ll 1$, the temperature profile is approximately linear because heat is transferred by conduction. When $H \gg 1$, vapour flow becomes the dominant mode of heat transfer and most of the evaporation occurs near the pipe end. As a result, the pipe temperature T_p drops sharply near the end within a thin boundary layer. Outside the boundary layer, there is little evaporation and T_p is again linear.

Figure 6(*b*) presents the normalized temperature along the pipe for $H = 100$, $R = 1$, and $S = 10^{-2}$, 10^{-1} and 1. It shows that as S increases, the slope of the outer temperature profile also increases. As a result, the temperature variation inside the boundary layer decreases. Since H and R are kept constant, the boundary-layer thickness remains the same for different S. The profiles for $S < 10^{-2}$ look almost the same as that for $S = 10^{-2}$. Since the two-dimensional analysis in the cross-sectional plane assumes a slender pipe, we require thet $S \ll 1$. Thus, we see that the pipe temperature distribution is insensitive to S if $S \ll 1$.

Figure 6(*c*) shows the effect of R on the normalized temperature along the pipe. The temperature profiles are calculated for $H = 100$, $S = 0.01$, and $R = 0.01$ to 10^4. It shows that the normalized temperature is almost linear when $R = 0.01$. As R increases, a boundary-layer begins to form near the pipe end. The boundary-layer thickness decreases as R increases, but the temperature variation inside the boundary layer also decreases. Thus, as $R \to \infty$, the boundary layer vanishes and the normalized temperature again becomes linear with unit slope. The effect of R can be understood as follows. When $R \ll 1$, the interfacial evaporation resistance is large, and heat is transferred mostly by conduction instead of vapour flow. This leads to a linear temperature profile along the pipe. As R increases, the evaporation resistance decreases, and it becomes easier for the liquid to evaporate. Most of the evaporation happens near the pipe end. Consequently, the temperature drops sharply within a thin boundary layer. When $R \gg 1$, the liquid evaporates almost exclusively at the end wall despite the small contact-line length. There is little evaporation elsewhere along the pipe, and, therefore, the pipe temperature is again linear, as shown by the case $R = 10^4$ in figure 6(*c*). Despite the linear temperature profile, heat is transferred predominately by vapour flow, leading to $Nu \gg 1$.

8. Vapour pressure variation along the pipe

The vapour pressure p_g can be determined from (6.11) between p_g and T_p and the solution of T_p in (7.2). The vapour pressure P_h at the hot end $z = L$ is found as

$$P_h - P_0 = \left(\frac{Nu - 1}{H}\right) \frac{\rho_0 h_{fg}}{T_0} (T_h - T_0), \tag{8.1}$$

where P_0 is the initial equilibrium vapour pressure which is also the vapour pressure at $z = 0$. The pressure difference $P_h - P_0$ is used to normalize the vapour pressure:

$$\frac{p_g - P_0}{P_h - P_0} = \frac{1}{1 + H} \left\{ \frac{NuH}{(Nu - 1)} \left(\frac{z}{L}\right) - \frac{(1 + H - Nu)}{(Nu - 1)} \frac{\sinh\left[(1 + H)^{1/2} R^{1/2} z/L\right]}{\sinh\left[(1 + H)^{1/2} R^{1/2}\right]} \right\}. \tag{8.2}$$

As $H \to 0$,

$$\frac{p_g - P_0}{P_h - P_0} \to \left[\frac{R^{1/2}\coth\left(R^{1/2}\right) + RS}{R^{1/2}\coth\left(R^{1/2}\right) + RS - 1}\right] \frac{z}{L} - \frac{\sinh\left(R^{1/2} z/L\right)/\sinh\left(R^{1/2}\right)}{R^{1/2}\coth\left(R^{1/2}\right) + RS - 1} + O(H). \tag{8.3a}$$

As $H \to \infty$,

$$\frac{p_g - P_0}{P_h - P_0} \to \frac{z}{L} + \frac{1}{RS} \left\{ \frac{z}{L} - \exp\left[-(HR)^{1/2}(1 - z/L)\right] \right\} H^{-1} + O\left(H^{-3/2}\right), \tag{8.3b}$$

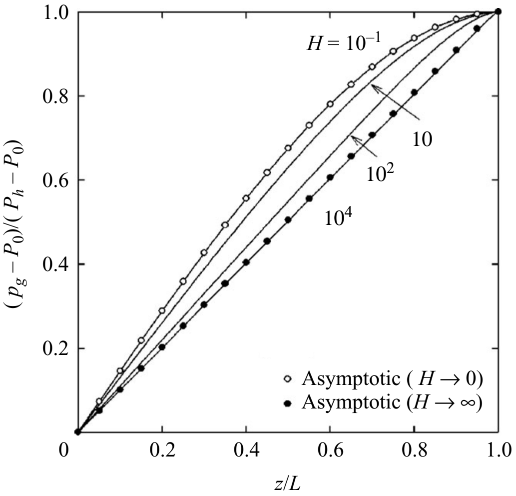

FIGURE 7. Normalized vapour pressure along the pipe for $S=0.01$, $R=1$ and various H. The exact solution (—) and its asymptotic expansions (symbols) are given in (8.2) and (8.3).

and there is no boundary layer near $z=L$. This is shown in figure 7 by plotting the normalized vapour pressure in (8.2) for $R=1$, $S=0.01$ and $H=0.1$ to 10^4. The asymptotic solutions in (8.3) are also plotted for $H=0.1$ and 10^4. It shows that when $H=10^4$, p_g varies almost linearly along the pipe. This is because for $H\gg 1$, most of the evaporation occurs at the pipe end inside the thermal boundary layer. Thus, the vapour flow is almost constant along the pipe, leading to the linear pressure gradient. For $H\ll 1$, there is continuous evaporation along the pipe and the vapour flow increases away from the pipe end. Thus, the pressure gradient also increases as z decreases, as shown in figure 7.

9. Vapour flow along the pipe

The vapour flow is driven by the vapour pressure gradient, as described by (6.4). Since the vapour pressure is known, the volume flow rate V_g can be found by differentiation. The flow rate at the middle of the pipe $z=0$ is denoted by V_0:

$$\frac{V_0}{C_g W^4(P_h-P_0)/(\mu_g L)}=\frac{-Nu}{(Nu-1)(1+H)}\left\{H-\frac{(1+H-Nu)(1+H)^{1/2}R^{1/2}}{Nu\sinh\left[(1+H)^{1/2}R^{1/2}\right]}\right\}. \tag{9.1}$$

At the hot end $z=L$, the flow rate V_h is found to be

$$\frac{V_h}{C_g W^4(P_h-P_0)/(\mu_g L)}=\frac{-Nu}{(Nu-1)(1+H)}\left\{H-\frac{(1+H-Nu)(1+H)^{1/2}R^{1/2}}{Nu\tanh\left[(1+H)^{1/2}R^{1/2}\right]}\right\}. \tag{9.2}$$

By comparing (9.1) and (9.2), we see that V_h differs from V_0 only by $\cosh[(1+H)^{1/2}R^{1/2}]$ inside the brackets. Hence, if $H\ll 1$ and $R\ll 1$, then $V_h\approx V_0$. The difference (V_h-V_0) is used to normalize V_g as

$$\frac{V_g-V_0}{V_h-V_0}=\frac{1-\cosh\left[(1+H)^{1/2}R^{1/2}z/L\right]}{1-\cosh\left[(1+H)^{1/2}R^{1/2}\right]}. \tag{9.3}$$

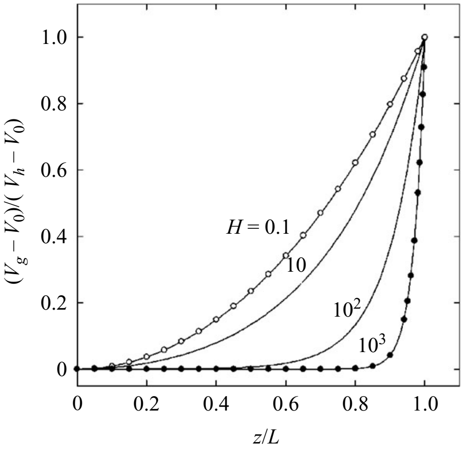

FIGURE 8. Normalized vapour volume flow rate along the pipe for $R = 1$ and various H. The exact solution (—) and its asymptotic expansions (symbols) are given in (9.3) and (9.4).

Thus, the normalized vapour flow rate is independent of S and depends only on H and R. As $H \to 0$,

$$\frac{V_g - V_0}{V_h - V_0} \to \frac{1 - \cosh\left(R^{1/2} z/L\right)}{1 - \cosh\left(R^{1/2}\right)} + O\left(H\right). \tag{9.4a}$$

As $H \to \infty$,

$$\frac{V_g - V_0}{V_h - V_0} \to \left[1 - \frac{R^{1/2}}{2}\left(1 - \frac{z}{L}\right) H^{-1/2}\right] \exp\left[-(HR)^{1/2}(1 - z/L)\right] + O(H^{-1}), \tag{9.4b}$$

which exhibits a boundary layer near the pipe end. The width of the boundary layer scales by $\delta z = (HR)^{1/2}$, which is the same as the thermal boundary layer. Outside the boundary layer, V_g approaches V_0. Figure 8 shows the normalized flow rate in (9.3) as a function of z for $R = 1$ and $H = 0.1$, 10, 10^2 and 10^3. The asymptotic solutions in (9.4) are also plotted for $H = 0.1$ and $H = 10^3$, and they represent the flow rate well at these values of H.

10. Liquid flow along the pipe

Since the pipe is a closed system, there is zero total mass flow at any point along the pipe:

$$\rho_f V_f + \rho_0 V_g = 0, \tag{10.1}$$

where V_f is the liquid volume flow rate in the z-direction. The vapour flow rate V_g has been determined in (9.3) so that

$$V_f = -\frac{\rho_0}{\rho_f} V_g. \tag{10.2}$$

Because the pipe is slender, we can treat the liquid flow along the pipe as unidirectional (White 2006) and

$$\frac{\mathrm{d}p_f}{\mathrm{d}z} = -\frac{\mu_f V_f}{C_f W^4}, \tag{10.3}$$

where the coefficient C_f depends on the shape of the flow domain and on the shear-stress boundary condition at the liquid–vapour interface. For the square domain shown in figure 2, $C_f = C_g = 0.5623$ if the interface is immobile, and $C_f = 1.830$ if the interface has zero stress (White 2006). Equation (10.3) together with (6.4) and (10.1) gives

$$\frac{\mathrm{d}p_f}{\mathrm{d}z} = -\frac{\mu_f \rho_0 C_g}{\mu_g \rho_f C_f}\frac{\mathrm{d}p_g}{\mathrm{d}z}. \tag{10.4}$$

Thus, the liquid pressure gradient is proportional to the vapour pressure gradient, but with an opposite sign. By imposing the boundary conditions $p_f = p_g = P_0$ at $z = 0$, we obtain

$$p_f = P_0 - \frac{\mu_f \rho_0 C_g}{\mu_g \rho_f C_f}(p_g - P_0), \tag{10.5}$$

where the vapour pressure p_g has been found in (8.2).

11. Interfacial curvature

The curvature of the liquid–vapour interface is determined by the Young–Laplace equation (Wong, Morris & Radke 1992):

$$p_g - p_f = \sigma\kappa, \tag{11.1}$$

where σ is the surface tension and κ is the curvature of the interface. Since the liquid pressure p_f is given in (10.5) and is proportional to the vapour pressure p_g, the curvature can be written as

$$\kappa = \left(1 + \frac{\mu_f \rho_0 C_g}{\mu_g \rho_f C_f}\right)\frac{(p_g - P_0)}{\sigma}. \tag{11.2}$$

Thus, the curvature behaves like the vapour pressure, which varies almost linearly for all values of R, H and S, as shown in figure 7.

The interfacial curvature is the last variable required in order to describe completely the fluid and heat flows in the pipe. From the analysis, we see that the driving force behind the operation of a micro heat pipe is the vapour pressure gradient generated by evaporation and condensation. The interfacial curvature plays a passive role in the heat transfer process. This is why we can take the interface as flat in the calculation of the vapour and liquid flows. In other words, we have performed a perturbation analysis in the limit of zero capillary number ($\mu_f U/\sigma$), and obtained the leading- and first-order expansions.

Previous models of micro heat pipes have focused on the interfacial curvature and liquid flow. Typically, a differential equation for κ is derived and solved by imposing various boundary conditions on κ. Here, we incorporate proper evaporation physics in our model and κ becomes passive. It exists only to balance the pressure jump across the interface, and no boundary condition on κ is required in order to arrive at the solution in (11.2). We find that the vapour pressure, which is usually neglected in previous models, is an important parameter. The liquid pressure is derived from the vapour pressure. Thus, the liquid flow and interfacial curvature are secondary in their relevancy to heat transfer compared with the vapour flow.

The interfacial curvature imposes a constraint on the temperature difference between the two ends of the pipe. Equation (11.2) shows that the maximum curvature κ_m occurs at the end of the pipe where $p_g = P_h$. In this work, we have assumed that the interface is approximately flat, i.e. $\kappa_m \ll W^{-1}$. This constraint on κ_m can be converted into a limit on $(T_h - T_0)$ using (8.1):

$$\frac{T_h - T_0}{T_0} \ll \frac{\sigma}{\rho_0 h_{fg} W} \left(\frac{H}{Nu - 1}\right) \left(1 + \frac{\mu_f \rho_0 C_g}{\mu_g \rho_f C_f}\right)^{-1}. \tag{11.3}$$

This condition makes explicit how small $(T_h - T_0)$ need be for our analysis to hold.

12. Discussion

The first part of this work studies fluid motion and heat transfer in a cross-sectional plane of the dual-wet micro heat pipe. Velocity, pressure and temperature gradients in the axial direction are assumed negligible compared with the in-plane gradients. This is valid if the length of the pipe is much longer than its width. Thus, the results obtained in § 2 to 5 are the leading-order solutions in the limit $L/W \to \infty$.

When we analyse liquid flow and heat transfer in the cross-sectional plane, the two-dimensional domain is taken to be unbounded vertically (figure 3). Liquid is assumed to enter at the bottom and leave at the top as vapour. This assumption of unbounded domain does not affect the results significantly. As shown in § 4, the interfacial temperature has an inner and outer structure. The inner region is not affected by the domain shape. The outer solution does depend on the domain shape, and the unbounded domain allows an analytical solution of the temperature field. However, since the dominant contribution to evaporation comes from the inner region, and this dominant evaporation term can be the only term used in § 6 to 11, the unbounded-domain assumption does not affect the final solution. It also has no effect on the liquid motion induced by evaporation and the Marangoni stress, because these flows to leading order in E^{-1} occur only in the inner region (see the Appendix). Hence, the simplification gained from the assumption of unbounded domain justifies its usage.

Convective heat transfer is negligible in the two-dimensional problem because the Péclet number $Pe \ll 1$. The Péclet number ($Pe = UMW/\alpha_T E$, where α_T is the liquid thermal diffusivity) measures the ratio of convective to conductive heat transfer. This Péclet number is defined using the Marangoni velocity UM (which is an order larger than the evaporative velocity scale U) and the length scale $E^{-1}W$ in the inner region (because the Marangoni flow is non-zero only in the inner region). We can estimate the Evaporation number E and the Marangoni number M for our dual-wet micro heat pipe using experimentally measured values in table 1: $E = 1820$ and $M = 38.9$. The velocity scale U in (3.1) is proportional to $p_e - p_g$, which peaks at the pipe end. Thus, the maximum velocity scale is

$$U_m = \frac{c}{\rho_f}(p_e - P_h) = \frac{c\rho_0 h_{fg}(H - Nu + 1)}{\rho_f H}\left(\frac{T_h - T_0}{T_0}\right), \tag{12.1}$$

where p_e in (6.2) and $(P_h - P_0)$ in (8.1) have been substituted. For our analysis to be valid, the temperature difference $T_h - T_0$ must obey (11.3). This means

$$U_m \ll \frac{c\sigma(H - Nu + 1)}{\rho_f W (Nu - 1)}\left(1 + \frac{\mu_f \rho_0 C_g}{\mu_g \rho_f C_f}\right)^{-1}, \tag{12.2}$$

which translates into $Pe \ll 1.02$, where we have taken $\alpha_T = 1.07 \times 10^{-7}\ \mathrm{m^2\,s^{-1}}$ for methanol, $C_f = C_g$, and $H = 0$. Other parameter values are given in table 1. Thus, convective heat transfer is indeed negligible in the two-dimensional problem.

Parameters	Experiment P1	Experiment P2	Experiment LB1	Experiment LB2	Dual-wet
W $(\times 10^{-6}\,\mathrm{m})$	22.5	30.0	61.0	126	50
L $(\times 10^{-3}\,\mathrm{m})$	10.0	10.0	10.0	10.0	25
A_f $(\times 10^{-9}\,\mathrm{m}^2)$	0.198	0.631	2.50	16.4	10
A_w $(\times 10^{-6}\,\mathrm{m}^2)$	0.190	0.252	0.235	0.512	0.2
T_0 (K)	315.0	310.0	325.0	317.0	300
μ_g $(\times 10^{-5}\,\mathrm{kg\,m^{-1}\,s^{-1}})$	1.00	1.00	1.08	1.00	1.00
μ_f $(\times 10^{-5}\,\mathrm{kg\,m^{-1}\,s^{-1}})$	58.4	58.4	67.7	42.6	58.4
$\sigma(\times 10^{-3}\mathrm{N\,m^{-1}})$	22.6	22.6	17.7	22.6	22.6
$\dfrac{\mathrm{d}\sigma}{\mathrm{d}T}(\times 10^{-3}\,\mathrm{N\,m^{-1}\,K^{-1}})$	−0.190	−0.190	−0.080	−0.190	−0.190
ρ_e or ρ_0 $(\mathrm{kg\,m^{-3}})$	1.29	1.29	1.44	1.29	1.29
ρ_f $(\mathrm{kg\,m^{-3}})$	791	791	760	791	791
h_{fg} $(\times 10^3\,\mathrm{J\,kg^{-1}})$	1100	1100	846	1100	1100
k_w $(\mathrm{W\,m^{-1}\,K^{-1}})$	148	148	148	148	148
k_f $(\mathrm{W\,m^{-1}\,K^{-1}})$	0.200	0.200	0.177	0.194	0.200
$c(\mathrm{s\,m^{-1}})$	0.00140	0.00140	0.00165	0.00140	0.0014
C_g	1.54	0.671	0.692	0.661	0.5623
α	1.00	1.00	1.00	1.00	1.00
E	780	1060	1800	4480	1820
M	40.8	40.2	14.5	56.3	38.9
S	0.00225	0.00300	0.00610	0.0126	0.002
R	0.673	0.503	0.0418	0.00196	0.506
H	8.97	9.47	116	1400	79.7

W is defined as the radius of the largest inscribed sphere for the triangular and rectangular pipes.
A_f for the four experiments is calculated assuming two-dimensional equilibrium circular meniscus (equation (A1) in Wong *et al.* 1995).
C_g is found assuming that the unidirectional vapour flow occupies the complete cross-sectional area.
E and M are calculated using (3.9) with T_p replaced by T_0.

TABLE 1. Two experiments from Peterson *et al* (1993) (P1 and P2), two from Le Berre *et al.* (2003) (LB1 and LB2), and a dual-wet micro heat pipe.

The inertia effect is also negligible in the two-dimensional problem because the Reynolds number ($Re = \rho_f UMW/\mu_f E$) is small. The Marangoni velocity MU and the inner length scale $E^{-1}W$ are again used. The constraint on the maximum velocity scale in (12.2) gives $Re \ll 0.15$, assuming again $C_f = C_g$ and $H = 0$, and using the parameter values from table 1. Thus, the inertia effect is negligible in the two-dimensional problem. Furthermore, the Marangoni flow is decoupled from the evaporation-induced flow, and thus any inertia effect on the Marangoni flow will have no effect on the evaporation rate.

Gravity is also not important in the two-dimensional problem because the interface is almost flat and because the temperature variation is small so that buoyancy can be neglected.

The total evaporation rate in a cross-sectional plane of the dual-wet micro heat pipe is of order $E^{-1}\ln E$, which comes from the inner region near the contact line. The normalized temperature varies smoothly in the inner region from 1 at the wall to 0 away from the wall. This is a result of the kinetic equation of evaporation. Without the kinetic equation, a non-integrable singularity in temperature appears at the contact line; the temperature jumps at the contact line from 1 at the wall to 0 at the interface. The wall is assumed isothermal, but this is not the reason for the inner region to exist. Even if the isothermal condition is imposed at a distance away from the solid–liquid interface, the inner region still persists (Morris 2000). The inner region also exists if the contact angle is decreased from 90° to 0 (Morris 2000; Ajaev & Homsy 2006). Thus, the inner region is intrinsic to evaporation near a solid wall.

The equilibrium vapour pressure at the hot end of a micro heat pipe is higher than that at the cold end, and this pressure difference is the basic driving force behind the operation of the pipe. Because the vapour can flow from the hot end to the cold end, the vapour pressure at the hot end cannot maintain the equilibrium value; this drop in vapour pressure below the equilibrium value induces continuous evaporation at the hot end. From the two-dimensional analysis at a cross-sectional plane, we find that the interfacial evaporation comes mainly from a small region near the contact line. We assume that a similar process occurs near the cold end, i.e. the vapour condenses in the inner region of the interface. As a result, the temperature and pressure distributions along the pipe are skew-symmetric about the mid-point of the pipe. There are other modes of condensation on a wall, such as drop-wise or film-wise condensation (Carey 1992). However, since the upper pipe wall is non-wetting, it is difficult to form a continuous film. Even if a droplet is formed on the wall, it will have high surface curvature given the large contact angle, and the drop pressure will be much higher than the vapour pressure. This will make continuous deposition on the droplet unfavourable (Carey 1992). Thus, the drop-wise condensation will have negligible contribution. Therefore, the problem discussed here is skew-symmetric, and only half of the micro heat pipe is considered.

An effective thermal conductivity can be defined for the dual-wet pipe as

$$k_e = \frac{qL}{A_T\,(T_h - T_0)} = \left(\frac{A_w k_w + A_f k_f}{A_T}\right)\frac{q}{q_c}, \tag{12.3}$$

where A_T is the total cross-sectional area including the liquid, vapour, and wall. The heat rate ratio q/q_c $(= Nu)$ depends on three dimensionless numbers: the heat-pipe number H, the interfacial evaporation resistance ratio R, and the aspect ratio of the pipe S, as given in (7.4). Figure 5 shows that $Nu \gg 1$ for $HR \gg 1$. Thus, k_e can be much larger than either k_w or k_f if the pipe is constructed and operated with the proper values of H, R, and S. Furthermore, these dimensionless numbers are independent of the temperature difference $(T_h - T_0)$ between the two ends of the pipe. Thus, driving the pipe at larger temperature differences will not improve the effective thermal conductivity. An effective heat transfer coefficient h_e can also be defined as

$$h_e = \frac{q}{A_T\,(T_h - T_0)} = \frac{k_e}{L}. \tag{12.4}$$

A thermal boundary layer appears near the pipe end as the heat-pipe number $H \to \infty$. The width of the layer scales as $(HR)^{-1/2}L$, which becomes vanishingly small as $H \to \infty$. However, § 2 to 5 we have assumed that the axial gradients are negligible compared with the cross-stream gradients, and § 6 to 11 we have taken the temperature variation along the pipe to be one-dimensional. This is correct if the axial variation of T_p occurs in a length scale that is large compared with the pipe width W. Thus, for our analysis to be valid, $(HR)^{-1/2}L \gg W$. This sets an upper bound on H.

The thermal boundary layer is an indicator of effective heat transfer in micro heat pipes. This is because the boundary layer only appears when vapour flow becomes the dominant mode of heat transfer. When vapour flow dominates, most of the evaporation occurs near the pipe end, so that the temperature drops rapidly within a thin boundary layer (figure 6). The case of $R = 10^4$ in figure 6(c) yields a linear temperature profile along the pipe even though vapour flow dominates. As explained in § 7, this unusual behaviour is caused by evaporation at the endwall. At such a large R value, there is negligible resistance for liquid to evaporate, and thus almost all the evaporation occurs at the endwall, despite the small contact-line length. The large heat flux carried by the vapour flow demands a large temperature drop just outside the pipe end. Thus, the linear temperature profile for $R = 10^4$ is caused by the pipe having an endwall with zero thickness. If the endwall has finite thickness, we expect to see a thermal boundary layer for $R \gg 1$ and $H \gg 1$. Hence, as a general rule, the existence of a thermal boundary layer is an indicator of effective heat transfer in micro heat pipes.

Two micro-heat-pipe arrays were constructed in silicon by Peterson *et al.* (1993) and tested using methanol as the working fluid. One is made of 39 rectangular channels each 45 μm wide, 80 μm deep, and 19.7 mm long in a silicon wafer 0.378 mm thick (experiment P1). The other is made of 39 triangular channels each 120 μm wide, 80 μm deep and 20 mm long in a silicon wafer 0.5 mm thick (experiment P2). The wafer was heated at one end to different temperatures depending on the input power. At the other end, the wafer was cooled to $15\,^{\circ}C$. Le Berre *et al.* (2003) built two types of micro-heat-pipe arrays in silicon wafers using ethanol or methanol as the working fluid. One of the arrays has 55 triangular channels each 230 μm wide, 170 μm deep and 20 mm long and with a spacing of 130 μm between two neighbouring channels. The void fraction in the transverse cross-section of the whole array is 8% (experiment LB1). The other array has 25 triangular channels; each is 500 μm wide, 340 μm deep and 20 mm long, and is attached to a smaller side channel (also triangular). The main triangular channels were filled with vapour and the side channels with liquid. We take the size of the side channel to be a quarter of that of the triangular main channel. The void fraction in the transverse cross-section of the whole array is 15% (experiment LB2). Table 1 gives the geometric and physical parameters for the four experiments. From the parameters, we can calculate E, M, S, R and H. We find that for all the experiments, $E \gg 1$ and $M \gg 1$. This justifies the expansions in the two-dimensional analysis. For experiment P1 and P2, $R \approx 0.5$ and $H \approx 9$. This is consistent with the observed linear temperature profile along the channels because $HR \sim 1$. For experiment LB1, $H = 116$ and $R = 0.0418$, and for experiment LB2, $H = 1400$ and $R = 0.00196$. The observed temperature profile is linear in LB1 and shows a small drop near the hot end in LB2. Although the product $HR \sim 1$ in both LB1 and LB2, the large H value in LB2 suggests probable heat transfer by vapour flow, and therefore the emergence of a thermal boundary layer.

13. Conclusions

A dual-wet micro heat pipe is proposed with simplified interfacial geometry while retaining the essential physics. Sections 2 to 5 study fluid motion and heat conduction in a cross-section plane in the heated half of the pipe. The wall temperature T_p is assumed known and the vapour pressure p_g is decreased below the equilibrium vapour pressure p_e to induce evaporation. Two dimensionless parameters emerge: E and M, and the problem is solved in the limits $E \to \infty$ and $M \to \infty$. The temperature field has an inner region near the contact line defined by the length scale $E^{-1}W$. This inner region is intrinsic to evaporation near a contact line and is independent of the outer domain shape. In the inner region, the dimensionless interfacial temperature varies smoothly from 1 at the wall to 0 away from the wall. This creates a Marangoni flow and an evaporation-induced flow, which are solved at different levels of expansion in M. It is found that the total evaporation rate $Q^* \sim E^{-1} \ln E$ to leading order. This is the evaporation rate per unit contact-line length.

Sections 6 to 11 determine the temperature distribution and vapour and liquid flows along the pipe. Thermal energy is transferred along the pipe by vapour flow (latent heat) and by conduction in the liquid and wall. These two modes of heat transfer always add up to a constant (q) at every point along the pipe because the pipe is insulated at the outer wall. The two transfer modes are coupled by the local evaporation rate Q found in §2 to 5. The evaporation rate Q depends on the local vapour pressure p_g and pipe (liquid and wall) temperature T_p. This is an important finding of our analysis because it leads to a thermal boundary layer near the pipe end.

Analytical solutions are found for all dependent variables: T_p (pipe temperature), p_g (vapour pressure), V_g (vapour flow rate), p_f (liquid pressure), V_f (liquid flow rate), and κ (interfacial curvature). The solutions depend on three dimensionless parameters: H, R, and S. If $HR \gg 1$, a thermal boundary layer appears near the pipe end in which the pipe temperature T_p varies rapidly (figure 6). The width of the layer scales as $(HR)^{-1/2}L$. A similar boundary layer exists at the cold end. Outside the boundary layers, T_p varies linearly with a gradual slope. Thus, these regions correspond to the evaporative, adiabatic and condensing regions commonly observed in heat pipes. This is the first time that the distinct regions are captured by a single temperature distribution, without prior assumptions of their existence. If $HR \sim 1$ or less, then T_p decreases almost linearly from the hot end to the cold. We analyse four micro-heat-pipe arrays studied experimentally and find $HR \sim 1$ (table 1). This explains the absence of the adiabatic region in most of those micro heat pipes.

The vapour pressure p_g varies almost linearly along the pipe and is insensitive to the value of H (figure 7), whereas a boundary layer exists for the vapour flow rate V_g for $H \gg 1$ (figure 8). The liquid volume flow rate V_f is proportional to V_g at every point along the pipe because the pipe is a closed system. The liquid pressure p_f is found from V_f and is therefore proportional to p_g. The difference $p_g - p_f$ gives the interfacial curvature κ, which varies almost linearly along the pipe and is also insensitive to H. Our analysis shows that the operation of a micro heat pipe is driven by the vapour pressure difference between the hot and cold ends. The interfacial curvature plays a passive role in the heat transfer process, contrary to conventional beliefs.

The heat rate q is constant along the pipe because the pipe is assumed to be insulated at the outer wall. An analytic solution is found for $Nu = q/q_c$, where q_c is the conductive heat rate through the pipe. We find that as $H \to \infty$, $Nu \sim H$, and as $H \to 0$, $Nu \to 1$ (figure 5). Thus, micro heat pipes should be designed and operated with $HR \gg 1$ to benefit from the evaporative heat transfer.

This work was supported by NASA (NAG3-2361 to H. W.), Louisiana Space Consortium (LaSPACE) Research Enhancement Awards (to H. W.), and a Louisiana Economic Development Award (to J. Z.).

Appendix A. Velocity field in the cross-sectional plane

The velocity field in the cross-sectional plane is expanded in the limit $M \to \infty$ as

$$\boldsymbol{u}^* = \boldsymbol{u}_0 M + \boldsymbol{u}_1 + \cdots \tag{A 1}$$

The velocity expansions $\boldsymbol{u}_0$ and $\boldsymbol{u}_1$ are zero in the outer region $x^* \gg E^{-1}$ and $y^* \gg E^{-1}$ defined in § 4. These velocity expansions in the limit $M \to \infty$ are also the zero-order term in the expansion in the limit $E \to \infty$. However, to zero order in E^{-1}, the liquid velocity is zero in the outer region; the velocity components are zero at the wall as stated in (3.6), at the symmetry plane as stated in (3.7), and at the interface as stated in (3.8) (because $t_0 = 0$ and $\partial t_0/\partial x^* = 0$ at the interface). Also, in (3.10*a*), the total evaporation rate $Q^* \sim E^{-1}$ in the outer region as shown in § 5, which means that $Q^* = 0$ to zero order in E^{-1}. Hence, $\boldsymbol{u}_0$ and $\boldsymbol{u}_1$ are zero in the outer region, and only their solutions in the inner region are studied below.

A.1. *Zero-order velocity $\boldsymbol{u}_0$ in the inner region*

In component form, $\boldsymbol{u}_0 = u_0\boldsymbol{i} + v_0\boldsymbol{j}$. At the liquid–vapour interface $Y = 0$, (3.8) gives

$$v_0 = 0, \quad \frac{\partial u_0}{\partial Y} = \frac{\partial \tau}{\partial X}. \tag{A 2}$$

Thus, there is zero evaporation at this order, and the flow is driven by the Marangoni stress.

A stream function is defined in terms of the inner variables:

$$u_0 = \frac{\partial \psi_0}{\partial Y}, \quad v_0 = -\frac{\partial \psi_0}{\partial X}. \tag{A 3}$$

The streamfunction obeys

$$\nabla^4 \psi_0 = 0. \tag{A 4}$$

No slip at the wall $X = 0$ requires

$$\psi_0 = 0, \quad \frac{\partial \psi_0}{\partial X} = 0. \tag{A 5}$$

At the liquid–vapour interface $Y = 0$, (A2) becomes

$$\psi_0 = 0, \quad \frac{\partial^2 \psi_0}{\partial Y^2} = \frac{\partial \tau}{\partial X}. \tag{A 6}$$

The velocity components decay to zero far from the corner. Thus, as $X \to \infty$ or $Y \to \infty$,

$$\frac{\partial \psi_0}{\partial Y} \to 0, \quad \frac{\partial \psi_0}{\partial X} \to 0. \tag{A 7}$$

The Marangoni stress at the interface is the only non-zero term and it drives the flow.

The unbounded domain is treated in two ways. First, coordinates X and Y are exponentially contracted by defining

$$\xi = \ln(X+1), \quad \eta = \ln(Y+1). \tag{A 8}$$

Secondly, a far-field asymptotic solution is found and used as boundary conditions at large but finite (ξ, η). The shear stress at the interface is non-zero near the corner, and decays to zero far from the corner, as shown by (A6). Thus, far from the corner, the shear stress can be viewed as a point force. The streamfunction generated by a point force pointing towards a solid wall is (Liron & Blake 1981)

$$\psi_0 = fY\left\{\frac{2DX}{Y^2+(X+D)^2} - \frac{1}{2}\ln\left[\frac{Y^2+(X+D)^2}{Y^2+(X-D)^2}\right]\right\}. \tag{A 9}$$

where f is the strength of the point force and D is the distance between the point force and the wall. The strength f is found from the shear stress boundary condition

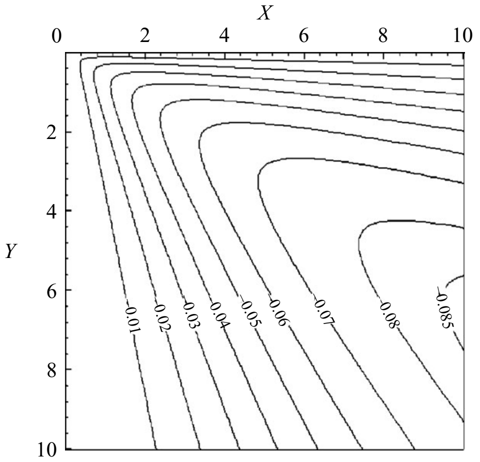

FIGURE 9. Streamlines of the Marangoni flow in the inner region. The X-axis is the liquid–vapour interface and the Y-axis is the wall surface. Liquid is dragged away from the hot wall by the Marangoni stress at the interface. The streamfunction $\psi_0=0$ at the wall and the interface and decreases away from the corner.

(A6) by integrating in X:

$$f=\frac{T\,(X_\infty)-1}{2\pi}, \tag{A 10}$$

where $X_\infty(\gg 1)$ is the position at which the boundary condition at infinity is applied. The distance D is determined from the first moment of the shear stress about $X=0$:

$$D=\left(\int_0^{X_\infty}\frac{\partial u_0}{\partial Y}\,\mathrm{d}X\right)^{-1}\left(\int_0^{X_\infty}X\frac{\partial u_0}{\partial Y}\,\mathrm{d}X\right). \tag{A 11}$$

The streamfunction is solved by a finite-difference method (Zhang 2002). The domain size is enlarged and the step size reduced until the solution converges. The streamlines are computed with domain size $(\xi,\eta)=$ (6, 6), (7, 7) and (8, 8), and with a step size ranging from 0.05 to 0.025 in ξ and η. The streamlines are shown in figure 9 and are accurate to four decimal places. An integral solution of (A4)–(A7) has been obtained by Tilley, Davis & Bankoff (2001).

A.2. *First-order velocity $\boldsymbol{u}_1$ in the inner region*

In component form, $\boldsymbol{u}_1=u_1\boldsymbol{i}+v_1\boldsymbol{j}$. A streamfunction ψ_1 is defined as

$$u_1=\frac{\partial\psi_1}{\partial Y},\quad v_1=-\frac{\partial\psi_1}{\partial X}. \tag{A 12}$$

This streamfunction solves

$$\nabla^4\psi_1=0, \tag{A 13}$$

and meets the no-slip boundary condition at the wall $X=0$:

$$\frac{\partial\psi_1}{\partial X}=0. \tag{A 14}$$

At the liquid–vapour interface $Y=0$, there is evaporation but no shear stress:

$$\frac{\partial\psi_1}{\partial X}=\tau=\frac{2}{\pi}X\int_0^{\infty}\frac{\mathrm{e}^{-\lambda}}{\lambda^2+X^2}\,\mathrm{d}\lambda, \tag{A 15a}$$

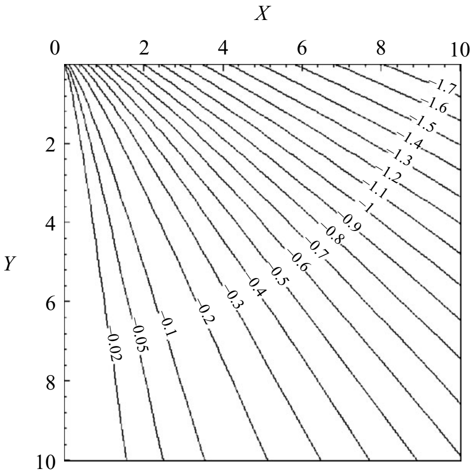

FIGURE 10. Streamlines of the evaporation-induced flow in the inner region near the contact line. The X-axis is the liquid–vapour interface and the Y-axis is the wall surface. The stream-function $\psi_1 = 0$ at the wall and decreases away from the wall.

$$\frac{\partial^2 \psi_1}{\partial Y^2} = 0. \tag{A 15b}$$

Far from the corner, as X or $Y \to \infty$,

$$\frac{\partial \psi_1}{\partial Y} \to 0, \quad \frac{\partial \psi_1}{\partial X} \to 0. \tag{A 16}$$

Thus, liquid flow at the first order is driven by evaporation at the interface.

The unbounded domain is treated by the same two methods: coordinate contraction as in (A8), and a far-field asymptotic solution. Evaporation at the interface occurs mainly near the wall, and decays to zero far from the wall. Thus, the liquid velocities far from the corner are the same as those of a sink flow. The radial velocity generated by a line sink on a planar wall is (White 2006)

$$u_r = -\frac{4F}{\pi r}\sin^2\theta, \tag{A 17}$$

where F is the sink strength or the volume flow rate per unit length, r is the radial distance, and θ starts from the wall. This sink flow applies because the interface acts like a symmetry plane. The sink strength is found by equating the leakage rates:

$$F = \int_0^{X_\infty} T_i(X, 0)\,\mathrm{d}X, \tag{A 18}$$

where X_∞ is the position of the outer domain boundary. Thus, at the outer domain boundaries,

$$\frac{\partial \psi_1}{\partial Y} = u_r \cos\theta, \quad \frac{\partial \psi_1}{\partial X} = -u_r \sin\theta. \tag{A 19}$$

The streamfunction is solved by a finite-difference method (Zhang 2002). The accuracy is verified by enlarging the domain and reducing the step size. The streamlines are computed with domain size $(\xi, \eta) = (5, 5)$, $(6, 6)$, $(7, 7)$ and $(8, 8)$, and with step size of 0.1, 0.05 or 0.0125 in ξ and η. The results are accurate to four decimal places. A plot of the streamlines is shown in figure 10.

REFERENCES

Ajaev, V. S. & Homsy, G. M. 2006 Modeling shapes and dynamics of confined bubbles. *Annu. Rev. Fluid Mech.* **38**, 277–307.

Badran, B., Gerner, F. M., Ramadas, P., Henderson, T. & Baker, K. W. 1997 Experimental results for low-temperature silicon micromachined micro heat pipe arrays using water and methanol as working fluids. *Experimental Heat Transfer* **10**, 253–272.

Barrett, J. & Clement, C. 1992 Kinetic evaporation and condensation rates and their coefficients. *J. Colloid Interface. Sci.* **150**, 352–364.

Burelbach, J. P., Bankoff, S. G. & Davis, S. H. 1988 Nonlinear stability of evaporating/condensing liquid films. *J. Fluid Mech.* **195**, 463–494.

Carey, V. P. 1992 *Liquid–vapor Phase-change Phenomena: An Introduction to the Thermophysics of Vaporization and Condensation Processes in Heat Transfer Equipment*. Taylor & Francis.

Churchill, R. V. & Brown, J. W. 1984 *Complex Varibales and Applications*. McGraw–Hill.

Cotter, T. R. 1984 Principles and properties of micro heat pipes. *Proc. Intl Heat Pipe Conf.* Tsukuba, Japan.

Darhuber, A., Troian, S. M. & Reisner, W. W. 2001 Dynamics of capillary spreading along hydrophilic microstripes. *Phys. Rev.* E **64**, 031603.

Faghri, A. 1995 *Heat Pipe Science and Technology*. Taylor & Francis.

Gau, H., Herminghaus, S., Lenz, P. & Lipowsky, R. 1999 Liquid morphologies on structured surfaces: from microchannels to microchips. *Science* **283**, 46–49.

Groll, M., Schneider, M., Sartre, V., Zaghdoudi, M. C. & Lallemand, M. 1998 Thermal control of electronic equipment by heat pipes. *Rev. Gen. Therm.* **37**, 323–352.

Ha, J. M. & Peterson, G. P. 1998 The heat transfer capacity of micro heat pipes. *Trans. ASME* C: *J. Heat Transfer* **120**, 1064–1071.

Khrustalev, D. & Faghri, A. 1994 Thermal analysis of a micro heat pipe. *Trans. ASME* C: *J. Heat Transfer* **116**, 189–198.

Launay, S., Sartre, V. & Lallemand, M. 2004 Hydrodynamic and thermal study of a water-filled micro-heat-pipe array. *J. Thermophys. Heat Transfer* **18**, 358–363.

Le Berre, M., Launay, S., Sartre, V. & Lallemand, M. 2003 Fabrication and experimental investigation of silicon micro heat pipes for cooling electronics. *J. Micromech. Microengng.* **13**, 436–441.

Levich, V. G. 1962 *Physicochemical Hydrodynamics*. Prentice–Hall.

Liron, N. & Blake, J. R. 1981 Existence of viscous eddies near boundaries. *J. Fluid Mech.* **107**, 109–129.

Longtin, J. P., Badran, B. & Gerner, F. M. 1994 A one-dimensional model of a micro heat pipe during steady-state operation. *J. Heat Transfer* **116**, 709–715.

Morris, S. J. S. 2000 A phenomenological model for the contact region of an evaporating meniscus on a superheated slab. *J. Fluid Mech.* **411**, 59–89.

Peterson, G. P. 1994 *An Introduction to Heat Pipes*. John Wiley.

Peterson, G. P., Duncan, A. B. & Weichold, M. H. 1993 Experimental investigation of micro heat pipes fabricated in silicon wafers. *J. Heat Transfer* **115**, 751–756.

Plesset, M. S. & Prosperetti, A. 1976 Flow of vapour in a liquid enclosure. *J. Fluid Mech.* **78**, 433–444.

Sobhan, C. B., Rag, R. L. & Peterson, G. P. 2007 A review and comparative study of the investigations on micro heat pipes. *Intl J. Energy Res.* **31**, 664–688.

Suman, B. & Kumar, P. 2005 An analytical model for fluid flow and heat transfer in a micro-heat pipe of polygonal shape. *Intl J. Heat Mass Transfer* **48**, 4498–4509.

Tilley, B. S., Davis, S. H. & Bankoff, S. G. 2001 Unsteady Stokes flow near an oscillating heated contact line. *J. Fluid Mech.* **438**, 339–362.

Wayner, P. C. 1993 Spreading of a liquid film with a finite contact angle by the evaporation/condensation process. *Langmuir* **9**, 294–299.

White, F. M. 2006 *Viscous Fluid Flow*. McGraw–Hill.

Wong, H., Morris, S. & Radke, C. J. 1992 Three-dimensional menisci in polygonal capillaries. *J. Colloid Interface Sci.* **148**, 317–336.

WONG, H., RADKE, C. J. & MORRIS, S. 1995 The motion of long bubbles in polygonal capillaries. 1. Thin films. *J. Fluid Mech.* **292**, 71–94.

WU, D. & PETERSON, G. P. 1991 Investigation of the transient characteristics of a micro heat pipe. J. Thermophys Heat Transfer **5**, 129–134.

WU, Q. & WONG, H. 2004 A slope-dependent disjoining pressure for non-zero contact angles. *J. Fluid Mech.* **506**, 157–185.

ZHANG, J. 2002 A model of heat and mass transfer in an idealized micro heat pipe. Master, Thesis, Louisiana State University.